

Enhancing Photovoltaic Performance Using an All-Conjugated Random Copolymer to Tailor Bulk and Interfacial Morphology of the P3HT:ICBA Active Layer

Anton Li, Jojo Amonoo, Bingyuan Huang, Peter K. Goldberg, Anne J. McNeil, and Peter F. Green*

Bulk heterojunction (BHJ) solar cells are fabricated using active material blends of poly(3-hexylthiophene) (P3HT) donor, indene-C₆₀ bisadduct (ICBA) acceptor, and an all-conjugated random copolymer (RCP) additive. By optimizing RCP loading, power conversion efficiencies (PCEs) up to 20% higher than those of a binary P3HT:ICBA mixture are achieved. The improved device characteristics are rationalized in terms of the differences between the photoactive thin film morphologies. Energy-filtered transmission electron microscopy reveals that incorporation of the RCP improves the degree of structural order of the BHJ fibrillar network and increases the extent of microphase separation between P3HT and ICBA. Additionally, a combination of atomic force microscopy and X-ray photoelectron spectroscopy analysis indicates segregation of the RCP at the free interface, leading to a shift in the surface potentials measured by Kelvin probe force microscopy. These changes, both in the bulk morphology and in the interfacial composition/energetics, are correlated to improved carrier collection efficiency due to a reduction of non-geminate recombination, which is measured by charge extraction of photo-generated carriers by linearly increasing voltage.

and carrier recombination processes. Another type of interface exists between the organic active layer and the typically inorganic electrode, which plays a critical role in carrier collection. In designing “optimal” morphologies for maximum power conversion efficiency (PCE), it is important to consider both the bulk internal morphology as well as interfacial structure/composition.

The morphology of the active layer BHJ is often described as a heterogeneous blend of crystalline aggregates/domains and amorphous phases with varying degrees of intermixing. Some miscibility between the components is necessary to maintain nanoscale domains and ensure that excitons can migrate to the D/A interface and dissociate into free carriers.^[1–3] Excessive intermixing, however, increases the sites and probability for non-geminate recombination and can suppress molecular ordering which facilitates carrier transport. Optimizing BHJ morphology

to strike a balance between carrier generation and transport is highly system-dependent and has been the subject of numerous experimental and computational studies.^[4–6] To this end, a wide range of strategies have been developed,^[7] including molecular design, choice of solvents and additives,^[8–10] and various annealing/post-processing techniques.^[11–14] More recently, there have been a number of studies on blending oligomer/polymer additives together with the active components as another means to tune the morphology. For example, small concentrations of copolymers additives have been added to poly(3-hexylthiophene (P3HT):phenyl-C₆₁ butyric acid methyl ester (PCBM) blends as compatibilizers or nanostructuring agents. Because the chemical constituents of the copolymers possess different affinities for the P3HT and PCBM components, the copolymers tend to segregate to the domain boundaries in order to minimize the free energy of the system. Consequently, incorporating them into the polymer/fullerene blend can alter the BHJ morphology (domain size, interfacial structure, extent of phase separation, etc.).^[15–19] This strategy has been deployed using rod-coil diblocks,^[20–23] and more recently, extended to all-conjugated copolymers of a range of architectures (block, gradient, random).^[24,25] Unfortunately, suppressing PCBM aggregate growth and increasing structural order have not always

1. Introduction

Polymer-based organic photovoltaics (OPVs) have garnered great interest due to their potential for low-cost and high-throughput roll-to-roll fabrication. Overall device performance is the product of carrier generation and transport processes which are heavily influenced by the morphology of the photoactive layer and its interfaces. On one hand are the donor/acceptor (D/A) interfaces associated with BHJ structure, which play host to both exciton dissociation

A. Li, B. Huang, Prof. P. F. Green
Department of Materials Science and Engineering
University of Michigan
Ann Arbor, MI 48109, USA
E-mail: pfgreen@umich.edu
J. Amonoo, Prof. P. F. Green
Applied Physics Program
University of Michigan
Ann Arbor, MI 48109, USA
P. K. Goldberg, Prof. A. J. McNeil
Department of Chemistry
University of Michigan
Ann Arbor, MI 48109, USA

DOI: 10.1002/adfm.201401058



translated into improved device performance, which may be partly due to the inclusion of non-conductive coil blocks.

In addition to the internal BHJ morphology, the nature of the active layer/electrode interfaces plays a vital role in device performance.^[26] While the maximum attainable open-circuit voltage (V_{OC}) of a device is governed by the energy difference between the highest occupied molecular orbital (HOMO) of the donor and the lowest unoccupied molecular orbital (LUMO) of the acceptor, voltage losses can be incurred by a variety of mechanisms at the electrode interfaces, which include extraction barriers, band bending, defect/trap states, etc. These effects typically also reduce carrier collection efficiency, manifesting as reduced short-circuit current (J_{SC}) and fill factor (FF).^[27–29] Thus, it has become widespread practice to insert another material between the active layer and electrodes; these interlayers can serve multiple purposes including work function alignment, selective carrier transport, and dipole formation/internal field enhancement.^[30] Traditionally, these interlayers have predominantly consisted of vacuum-deposited inorganic materials, but in recent years there has been a trend towards solution-processible materials compatible for roll-to-roll printing.^[31–33] For layer-by-layer deposition, however, the need for orthogonal solvents imposes significant limitations based on material solubilities.

Tailoring BHJ morphology and modifying electrode interfaces have usually been addressed as different questions requiring separate strategies, but in this study we show that altering the active layer composition can involve both aspects simultaneously. Herein, we introduce a fully-conjugated random copolymer additive, poly(3-hexylthiophene-*r*-3-((hexyloxy)methyl)thiophene), P(3HT-*r*-3HOMT), which simultaneously modifies the BHJ morphology and the active layer/electrode interface. We systematically incorporated varying concentrations of the random copolymer (RCP) into a blend of P3HT and indene- C_{60} bisadduct (ICBA),^[34–36] and found that device efficiencies improved substantially at optimized loading fractions. Both the internal and interfacial morphology of the active layer are characterized and correlated to the device performance. We conclude that the RCP plays an important role on two fronts, altering the D/A phase separation within the BHJ as well as segregating to the cathode contact, both of which facilitate collection of photogenerated carriers.

2. Results and Discussion

2.1. Characterization of Polymer/Copolymer Thin Films

Annealed films of P3HT, P3HOMT, and P(3HT-*r*-3HOMT) were characterized by UV-visible spectroscopy and conductive atomic force microscopy (c-AFM). The absorption profile of P3HOMT was found to be significantly blue-shifted from that of P3HT and the peaks associated with π -aggregation are absent (Figure 1). The apparent lack of extended π -conjugation in P3HOMT films suggests that the modified side chain disrupts alignment and packing of polymer chains, thus inhibiting crystallization and long-range ordering.^[37] The absorption profile of the random copolymer (RCP), on the other hand, closely resembles that of P3HT but is slightly blue-shifted. This result indicates that the suppressed ordering of P3HOMT chains is

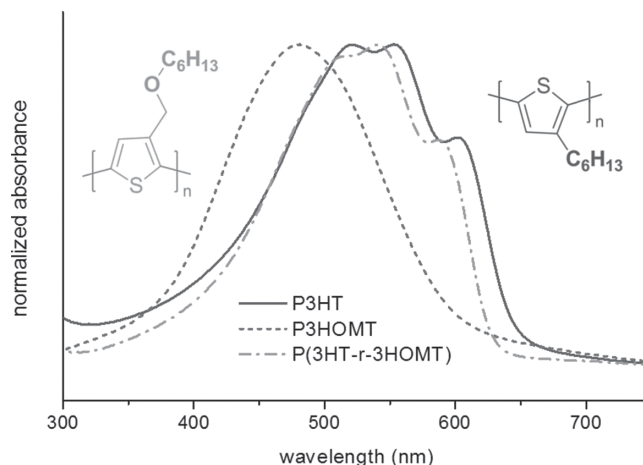


Figure 1. UV-vis absorption spectra of P3HT, P3HOMT, and P(3HT-*r*-3HOMT). Chemical structures of the two homopolymers are also shown.

mitigated when 3HT units are dispersed along the polymer chain.

As shown in Figure 2, AFM topographical scans of pure polymer films reveal that P3HOMT has a much smoother surface than P3HT (rms roughness of 0.8 nm versus 5.4 nm) and a comparatively featureless texture based on the friction map in Figure 2b. In contrast, the P(3HT-*r*-3HOMT) film exhibits a distinctive surface texture with fine lamellae-like features (Figure 2c), along with an intermediate surface roughness of 4.3 nm. These findings corroborate the UV-vis data, showing that P3HOMT remains largely amorphous even after annealing, whereas the RCP is capable of packing and reorganizing to produce a more semicrystalline film, although with a different surface structure from homopolymer P3HT film. The surface features can be seen even more clearly in the dark current maps (Figure 2d–f), and by plotting dark current measured at each pixel (under +3.0 V applied bias) in a histogram (Figure 2g), it is possible to gain a semi-quantitative sense of the relative carrier mobilities of each polymer. The P3HOMT is found to possess very low conductivity compared to P3HT, reflecting poor carrier transport through the disordered polymer chains of the amorphous film. The intermediate and broad distribution of current for P(3HT-*r*-3HOMT) confirms the ability of its chains to align and pack into some ordered structures that facilitate carrier transport, although to a lesser extent than homopolymer P3HT.

Even in the absence of enthalpic driving forces, entropic effects associated with differences in polymer chain flexibilities and crystallization behavior can lead to the preferential segregation of one component to the free surface.^[38–40] We evaluated the relative surface segregation affinities of P3HT, P3HOMT and P(3HT-*r*-3HOMT) by comparing the surface morphologies of blends to those of the pure components. As shown in Figure 3, the surface of the P3HT:P3HOMT blend appeared largely amorphous (Figure 3a,c), much like the pristine P3HOMT sample. Likewise, the surface of the P3HT:RCP blend (Figure 3b,d) exhibits a texture nearly identical to that of the pristine RCP film. These findings strongly suggest that P3HOMT and P(3HT-*r*-3HOMT) have a stronger tendency for

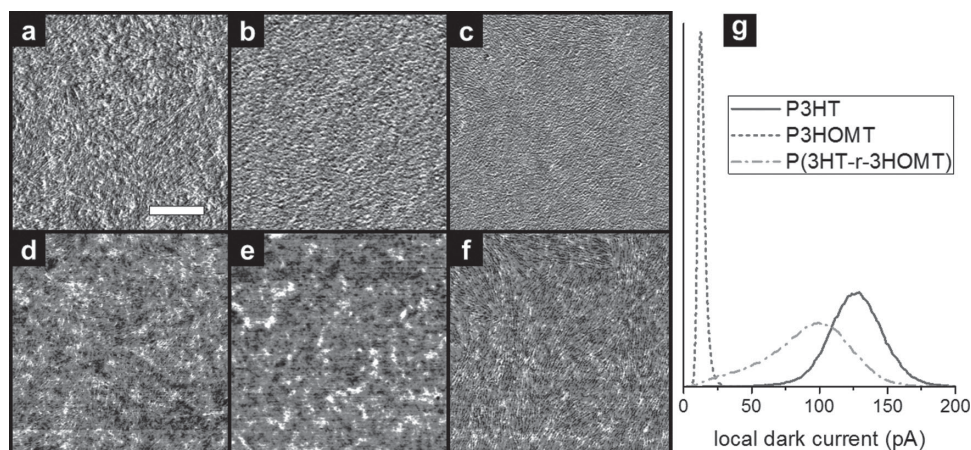


Figure 2. Phase (a–c) and dark current (d–f) micrographs for films of pure P3HT (a,d), P3HOMT (b,e) and RCP (c,f) (scale bar = 0.5 μm). The dark current values measured at each pixel of the c-AFM images are plotted in the histogram (g).

surface segregation than P3HT, which is consistent with their relatively lower degrees of crystallinity indicated by their optoelectronic properties.

2.2. Bulk Heterojunction Device Measurements

Having established some context for the characteristics and behavior of the RCP, we will now discuss its effect as an additive for P3HT:ICBA bulk heterojunction solar cells. For each RCP loading concentration from 0% to 20%, at least 8 devices were measured; representative J–V curves under illumination are shown in **Figure 4**, and the average values for the V_{OC} , J_{SC} , FF, and PCE are summarized in **Table 1**. The “champion” device

performance was achieved at a RCP loading concentration of 8 wt.%, producing a 20% increase in PCE (from 4.2% to 5.0%) over the reference device (0% RCP). This improvement is due in large part to a higher V_{OC} , which increases monotonically with RCP concentration. J_{SC} and FF show some improvement up to the optimal composition, but they decrease significantly at higher loadings. This deterioration is unsurprising considering the inferior carrier transport properties of P(3HT-r-3HOMT); while insignificant at low concentrations, the lower conductivity of the RCP is expected to increase the series resistance of the device more noticeably at higher loadings, hampering carrier transport through the active layer and decreasing photocurrent collection. Furthermore, as more RCP is added to the blend, the corresponding decrease in the total fraction of ICBA may reduce the connectivity of electron-transporting

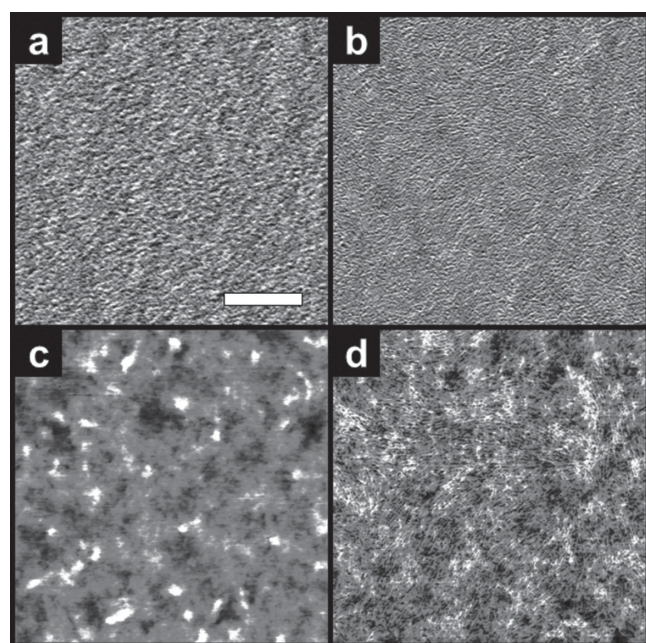


Figure 3. Phase (a,b) and dark current (c,d) micrographs for a P3HT:P3HOMT blend (a,c) and a P3HT:RCP blend (b,d) (scale bar = 0.5 μm).

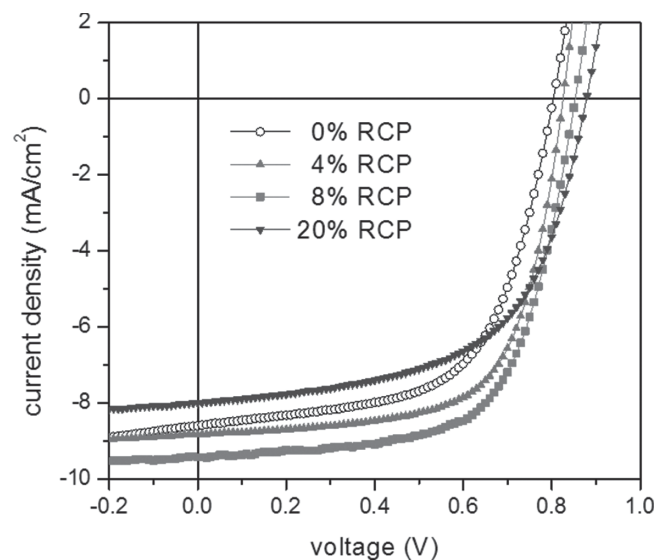


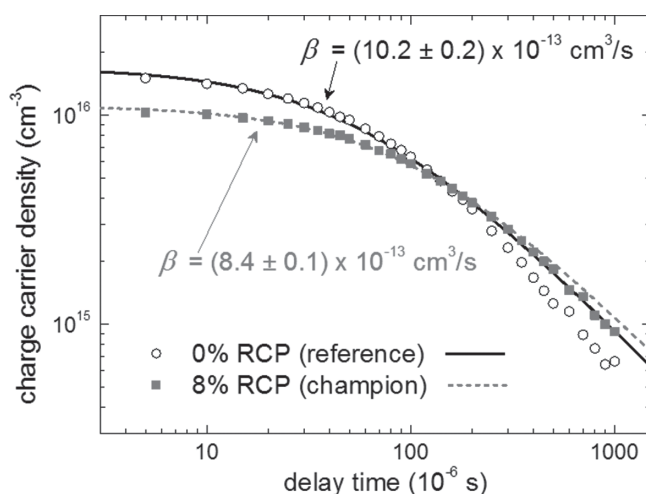
Figure 4. Representative J–V curves under illumination for devices fabricated from a range of RCP loadings (wt%). The curves for 0% RCP (open circles) and 8% RCP (filled squares) represent the performances of the reference and champion devices, respectively.

Table 1. Summary of device characteristics for different copolymer concentrations.

f_{RCP} [wt%]	V_{OC} [V]	J_{SC} [mA cm ⁻¹]	FF	PCE [%]
0	0.79 (±0.02)	8.7 (±0.4)	0.61 (±0.01)	4.2 (±0.2)
2	0.81 (±0.01)	8.4 (±0.3)	0.65 (±0.01)	4.4 (±0.2)
4	0.82 (±0.02)	8.3 (±0.2)	0.67 (±0.01)	4.5 (±0.1)
6	0.83 (±0.02)	8.8 (±0.4)	0.66 (±0.01)	4.8 (±0.2)
8	0.84 (±0.01)	9.1 (±0.2)	0.65 (±0.01)	5.0 (±0.1)
10	0.85 (±0.02)	9.1 (±0.3)	0.62 (±0.01)	4.7 (±0.1)
15	0.86 (±0.01)	8.6 (±0.2)	0.62 (±0.01)	4.6 (±0.1)
20	0.88 (±0.01)	8.0 (±0.2)	0.59 (±0.02)	4.2 (±0.1)

fullerene clusters/domains, leading to a decrease in photocurrent collection.^[3]

Carrier generation/recombination for reference (0% RCP) and champion (8% RCP) devices were characterized using photo-CELIV. Following laser pulse excitation, the transient current was measured at various delay times t to obtain photo-generated carrier density $n(t)$, shown in **Figure 5**. The recombination coefficient β was calculated by fitting the measured carrier densities to a bimolecular decay law for nondispersive recombination: $n(t) = n(0) \left[1 + (t/\tau_B) \right]^{-1}$, where $\tau_B = [n(0)\beta]^{-1}$.^[41] From this analysis, the reference device was found to have $n(0) = (1.70 \pm 0.3) \times 10^{-16} \text{ cm}^{-3}$ and $\beta = (10.2 \pm 0.1) \times 10^{-13} \text{ cm}^3 \text{ s}^{-1}$, while the champion device exhibited $n(0) = (1.11 \pm 0.1) \times 10^{-16} \text{ cm}^{-3}$ and $\beta = (8.4 \pm 0.1) \times 10^{-13} \text{ cm}^3 \text{ s}^{-1}$, indicating a reduction in both initial carrier generation and non-geminate recombination. It is important to note that while the bimolecular model provides a fairly good fit for the champion device, it significantly underestimates the rate of carrier decay in the reference device at longer delay times (>100 μs). This discrepancy suggests that the lower performance of the reference P3HT:ICBA devices may originate from additional recombination losses not

**Figure 5.** Carrier densities $n(t)$ measured by photo-CELIV for the reference (open circles) and champion (filled squares) devices following a delay time t after laser pulse excitation. The curves are the fits to a bimolecular decay law with recombination coefficient β .

described by bimolecular mechanism, such as trap-assisted or surface recombination. These findings will be revisited in the context of the active layer morphology, following the discussion of structural characterization.

2.3. Bulk Heterojunction Morphological Characterization

The bulk internal morphologies of device active layers were studied using energy-filtered transmission electron microscopy (EFTEM), taking advantage of the different electron energy-loss spectra (EELS) of P3HT and ICBA to distinguish polymer and fullerene-rich domains/phases.^[42,43] Unfortunately, the minority fraction of the RCP could not be identified in the EFTEM images, due to its similar chemical structure to P3HT and nearly identical EELS. However, a qualitative comparison of the images in **Figure 6** reveals that the active layer of the champion device (Figure 6b) displays more distinct and numerous P3HT fibrils (the dark features) and clearer contrast between the P3HT and ICBA-rich phases compared to the reference sample (Figure 6a). The relative difference in phase purities was further evaluated by analyzing the local EELS of P3HT and ICBA-rich regions, as described in the Experimental Section. Based on the plasmon peak energies, the incorporation of RCP may have slightly improved the relative purity of the P3HT domains (although the difference is small compared to the range of error) but significantly increased the relative purity of the ICBA-rich phase; the higher purity is consistent with the visually clearer contrast in the EFTEM image. This result suggests that in the reference sample, the fibrils are sparse, but they are already relatively pure in P3HT. With addition of the RCP in the champion sample, more of the P3HT “precipitated” out of the intermixed regions (thereby purifying the ICBA-rich phase) and aggregated into the more numerous fibrils.

Although the RCP cannot be spatially located in the EFTEM images, we can use polymer physics and thermodynamics to rationalize its influence on the phase behavior of the blend. It is well-established that, in order to minimize free energy, copolymers in amorphous polymer blends tend to either segregate to interfaces (between phases and/or at the surfaces) or form micelles, due to differences in relative interactions between each copolymer constituent and the components of the host blend.^[44,45] In a mixture of two immiscible polymers, the presence of the copolymer (with appropriately-selected constituents) at the phase boundaries lowers the interfacial tension between the two phases, which inhibits macroscale phase separation and stabilizes the morphology; for this reason, copolymers have often been employed in low concentrations as surfactants or compatibilizers for immiscible blends.^[46,47] It is worth noting that the systems investigated in this study differ in some respects from aforementioned immiscible polymer/polymer blends, due to the inherently high degree of intermixing between the P3HT and ICBA,^[36] along with the rigidity of conjugated polymer chains and the behavior of fullerene molecules. Nonetheless, we can reasonably infer that the RCP segregates to the interfacial regions between P3HT and ICBA-rich phases (there is little driving force for micelle formation, since the RCP possesses a random distribution of 3HT and 3HOMT units). At these interfaces, the 3HT components of the copolymer preferentially

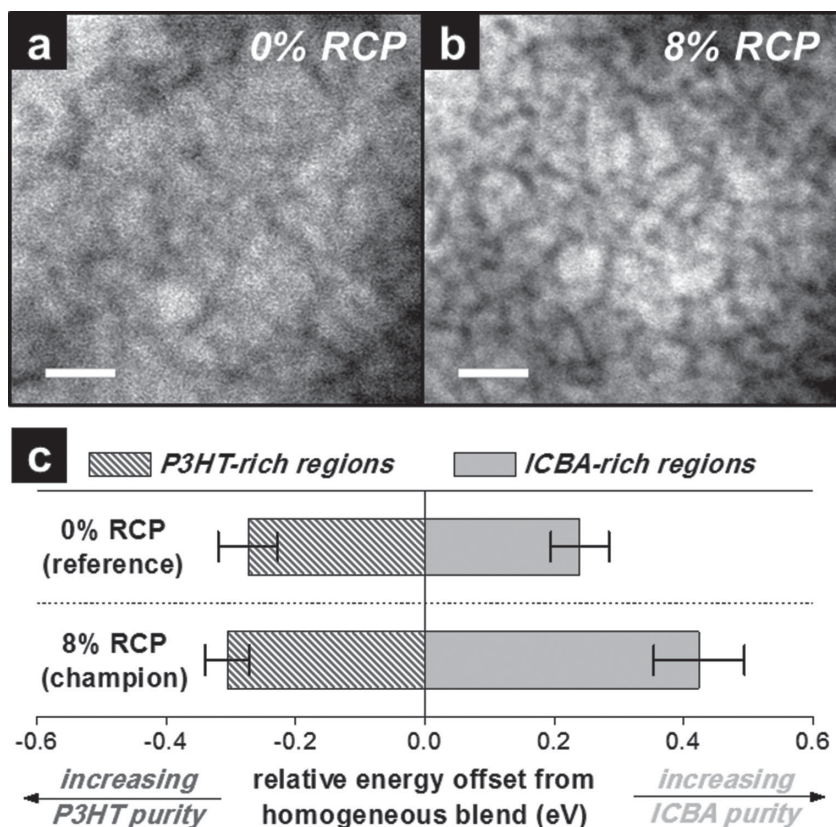


Figure 6. EFTEM images of the 0% RCP (a) and 8% RCP (b) active layers, taken at an energy-loss interval 31 ± 3 eV, such that the dark features correspond to P3HT-rich domains/fibrils and the bright regions correspond to the ICBA-rich phase (scale bar = 50 nm). The plot in (c) shows the difference in the plasmon peak energies between the overall EELS of the entire imaged area and the local EELS of P3HT- and ICBA-rich regions, respectively. A larger deviation from the overall EELS (corresponding to an averaged, homogenous blend) reflects higher phase purity.

interact with the P3HT homopolymer, and as a result, the covalently-bound 3HOMT components are also restricted to the boundaries of P3HT domains. Although the precise mechanism is unclear, the “encapsulation” of P3HT domains by the RCP could exclude ICBA molecules from infiltrating the polymer phase, giving rise to the observed enhancement in polymer/fullerene phase separation (purity). A similar effect was reported in recent computational work by Kipp and Ganesan, in which the addition of block copolymers to polymer/fullerene blends produced an increase in short-range phase separation in the equilibrium morphologies.^[48]

As previously alluded, in addition to the boundaries between phases/domains, interfacial segregation can also occur at the substrate and/or free surface of the film; in a device configuration, these correspond to the bottom and deposited electrodes, respectively. As previously shown, the RCP exhibits lower surface energy compared to P3HT, so we focused our attention on the free surface of the active layer, which contacts the deposited LiF/Al cathode in completed devices. In **Figure 7**, the AFM friction maps (Figure 7a insets) reveal that the reference sample possesses a rougher and coarser surface compared to the 8% RCP sample, which exhibits a fine lamellar texture strikingly similar to that of the pure RCP film (Figure 2c,f). To complement these AFM measurements, XPS was performed to detect

changes the composition of the active layer surface upon incorporation of the RCP. Both samples exhibited nearly identical, strong sulfur 2p peaks, consistent with studies which have shown the preferential surface segregation of P3HT in a polymer/fullerene blend.^[49] Although the chemical compositions of the two samples were nearly identical, the RCP uniquely possesses oxygen atoms (in the 3HOMT side chains). The oxygen 2s peak was too weak to extract useful information; instead we analyzed the carbon 1s peak around 285 eV, applying a number of fittings to separate the signal into peaks corresponding to specific types of bonds (Figure 7a). We find a significant increase in C–O bond density at the surface of the 8% RCP sample (the C–O peak in the reference sample likely originates from surface contaminants and oxidized species). The combination of AFM and XPS measurements provide strong evidence that the RCP preferentially segregates to the free surface, resulting in a RCP-rich interfacial layer in contact with the deposited cathode (Figure 7b).

2.4. Connecting Device Performance with Morphology

Numerous studies have shown that differences in BHJ morphology have important consequences on photocarrier generation and transport, which manifest as changes in the V_{OC} , J_{SC} , FF, and PCE of devices.^[50,51]

Simulations by Lyons et al. show that higher phase purity and sharper D/A interfaces reduces the available interfacial area for exciton dissociation, and thus the rate of carrier generation. Despite this, provided that the domains sizes are within the exciton diffusion length (~ 10 nm), this decrease is more than compensated by a much higher carrier collection efficiency due to reduced bimolecular recombination.^[52] These computational results are consistent with our EFTEM images and carrier recombination measurements: clearer contrast between P3HT and ICBA domains and a greater degree of structural order are correlated with a lower initial carrier density but slower recombination rate in the champion device. Furthermore, while the reference P3HT:ICBA device appears to suffer from recombination losses beyond the bimolecular mechanism, the champion device does not. One way to rationalize this observation is that in the reference device, not only does the higher degree of intermixing increase bimolecular recombination via the larger donor/acceptor interface, it also results in greater structural disorder which produces more gap states for trap-assisted recombination. The enhanced phase separation and improved structural order after incorporating the RCP led to a corresponding decrease in energetic disorder and trap density, thereby mitigating those losses. However, as previously discussed, the RCP is less conductive than P3HT homopolymer, so

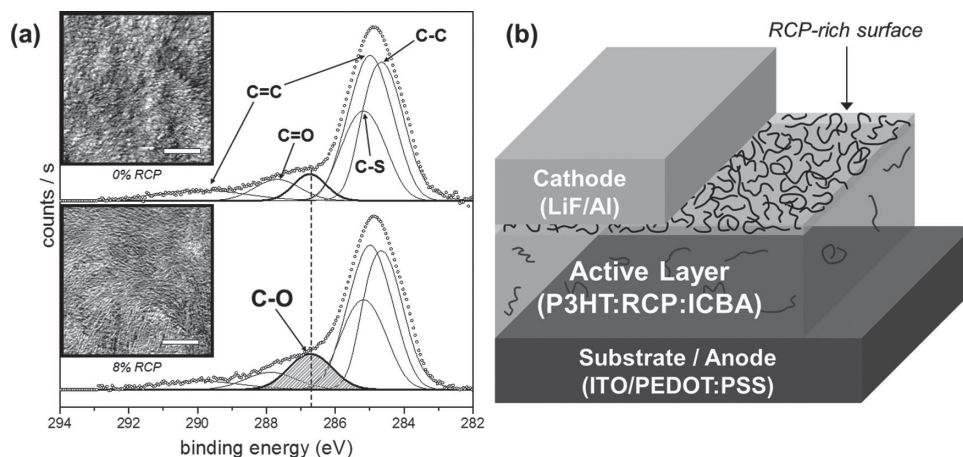


Figure 7. (a) Carbon 1s peak from XPS for the reference (0% RCP) and champion (8% RCP) devices, with corresponding AFM phase images shown in the insets (scale bar = 0.5 μm). The bolded curve with shading is the fitted peak corresponding to C–O ether bonds. (b) Diagram of the proposed surface segregation behavior of the RCP (represented by black lines) in the active layer of the device.

at high concentrations, excess copolymer impedes carrier transport and undermines the benefits conferred by the improved morphology. These competing phenomena contribute to the existence of an optimal RCP loading fraction.

While tailoring BHJ morphology can yield significant reductions in “bulk” recombination occurring within the active layer, changes to the film’s interfacial structure and composition also play a critical role in carrier collection at the electrodes. For the P3HT:ICBA devices in this study, fabricated in the conventional architecture, it is therefore highly probable that the RCP-rich surface layer had a strong influence on carrier transport from the active layer to the cathode. Indeed, in a complementary study, Ma et al. used the interfacial (substrate) segregation of an amine-functionalized fullerene to create a self-assembled cathode interlayer for inverted devices.^[53] In context of the carrier recombination findings from photo-CELIV, we propose that the enhanced device performance of the RCP-containing champion device is at least partly due to suppression of surface recombination at the cathode. Recall that the accelerated carrier decay in the reference device, which deviates from the bimolecular model prediction, occurred at longer delay times (onset ~ 100 μs); this time-lag could be associated with the time for photogenerated carriers to migrate to the cathode.

There are several mechanisms by which the surface-segregated RCP could aid in carrier extraction to reduce recombination at the interface. Its more amorphous character and the smoother film surface it forms could enable better physical contact with the cathode; another explanation could be that the oxygen-bearing side chains (weakly polar) of the RCP generate favorable interfacial dipoles. Although we do not exclude the possibility of these and other effects, in this study we focus on the influence of the copolymer on energy levels at the interface, employing Kelvin probe force microscopy (KPFM) to measure the surface potentials of active layers with and without RCP. Following the procedure described in the Experimental Section, the effective HOMO and LUMO energies of the blends were mapped, and the distributions of surface potential values plotted as a histogram in **Figure 8**, using a Gaussian fit to obtain representative HOMO/LUMO values for comparison (the corresponding KPFM images

can be found in the Supporting Information). It is worth emphasizing that this technique is highly sensitive to the energies of the species at the surface, but the measured potentials are influenced by the underlying film. Thus, the surface potentials of the blends cannot be directly correlated to the HOMO/LUMO of individual species, but are averaged to some extent over all the constituents of the blend; for this reason, the surface potentials measured for the blends are higher than the pure polymers, being shifted to higher energies by the HOMO of ICBA.

From this analysis, we found that the HOMO of the champion RCP-containing sample shows a significant downward shift of ~ 0.1 eV from the reference P3HT:ICBA sample. This offset closely mirrors the difference between the measured HOMO energies for films of pure P3HT and RCP (Figure 8 inset), which strongly suggests that the lower HOMO of the champion blend is due to the surface-segregated RCP. On the other hand, the LUMO energies of the two samples mostly overlapped, and while the RCP-containing sample showed a broader distribution of surface potentials, the peak values were almost identical. The broadening of surface LUMO energies could be ascribed to the more amorphous/disordered behavior of RCP chains, or to different electronic interactions between the molecular orbitals of RCP and ICBA, although the rigorous explanation is still unclear.

Nonetheless, based on the offset in HOMO levels, we propose that the surface-segregated RCP helps to suppress surface recombination by curbing migration of positive charge carriers to the cathode. Holes transported along the conjugated polymer domains/chains encounter the deeper HOMO of the RCP if they approach the interface. Under this scenario, this downward band bending decreases the probability of holes reaching the cathode and undergoing surface recombination with dissociated electrons. Although the RCP (and conjugated polymers in general) is primarily a hole-transporting material, electron extraction has been shown to be relatively unhindered provided that the polymer-rich interfacial layer is thin.^[54] A sufficient amount of copolymer is required to populate the internal and external interfaces, so the optimal loading of 8% RCP could be associated with the threshold concentration at which the polymer/fullerene interfaces become saturated and the cathode

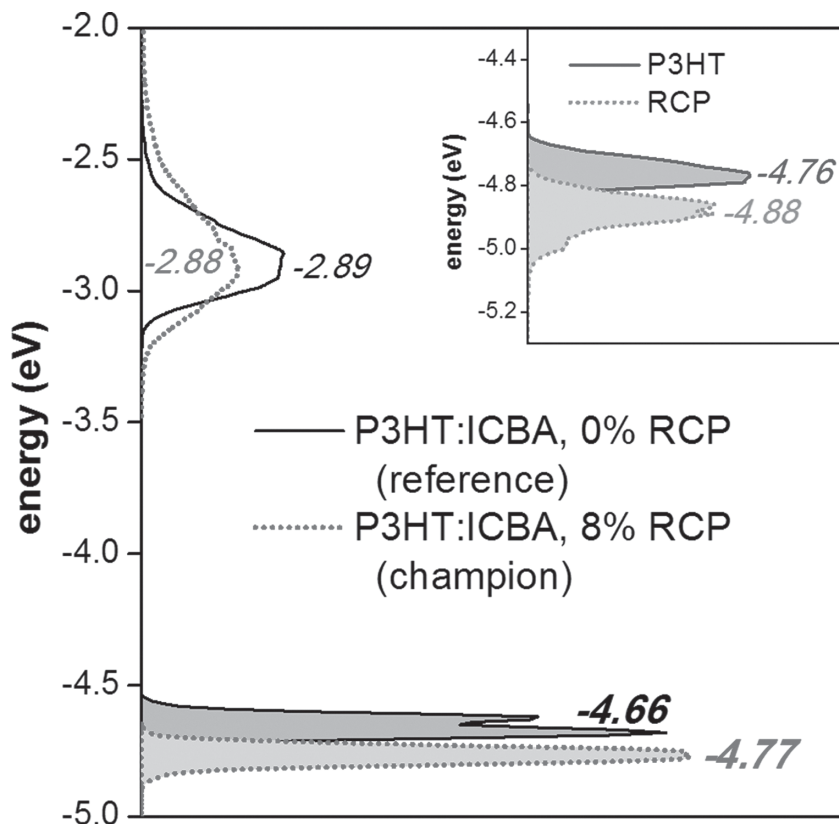


Figure 8. Surface potentials of the P3HT:ICBA active layer with and without RCP; the values measured at each pixel of the KPFM images are plotted as a histogram. The shaded distributions (lower) correspond to HOMO measurements and the unshaded distributions (upper) correspond to LUMO measurements. The values shown represent the energies of the peaks (from a Gaussian fit) of the respective HOMO/LUMO distributions. The inset histogram shows the HOMO surface potentials for pristine P3HT and RCP films.

contact is fully wetted. As even more RCP is added to the blend, besides potentially increasing the bulk series resistance of the device, further surface segregation may produce an excessively thick interfacial layer that acts as a barrier to electron extraction.

3. Conclusion

Having synthesized and characterized a fully-conjugated random copolymer, P(3HT-*r*-3HOMT), we incorporated it as an interfacially-active additive for P3HT:ICBA bulk heterojunction solar cells, achieving a 20% increase in PCE at the optimal loading concentration of 8 wt%. The influence of the copolymer on the active layer morphology was studied in detail, employing a wide range of techniques to investigate the film's internal morphology as well as interfacial structure and composition. The enhanced device performance is credited to a combination of two main structural factors: 1) a superior microphase-separated BHJ morphology that reduced internal bimolecular recombination losses and 2) a copolymer-rich active layer/cathode interface that suppressed surface recombination and improved charge collection efficiency. These findings present new insights and opportunities for to take advantage of the self-organizing behavior of copolymers to tune the morphology and properties

of polymeric thin films for OPVs and other applications.

4. Experimental Section

Polymer Synthesis: P3HOMT homopolymer and P(3HT-*r*-3HOMT) were synthesized by a nickel-catalyzed catalyst-transfer polycondensation using the monomers and catalyst described for P8 in the literature.^[55] The relative reactivities of the two monomer species are very similar and close to 1, yielding a random distribution along the chain (39:61 3HT:3HOMT ratio). Polymer molecular weights were determined using gel-permeation chromatography (GPC) by comparison with polystyrene standards (Varian, EasiCal PS-2 MW 580-377,400) on a Waters 1515 HPLC instrument equipped with Waters Styragel (7.8 × 300 mm) THF HR 0.5, THF HR 1, and THF HR 4 type columns in sequence and analyzed with Waters 2487 dual absorbance detector (254 nm). Samples were dissolved in THF (with mild heating) and passed through a 0.2 μm PTFE filter prior to analysis. For P3HOMT, it was found that $M_n = 16.2$ kDa, PDI = 2.19, and regioregularity = 97%; for P(3HT-*r*-3HOMT), $M_n = 38.0$ kDa, PDI = 1.99, regioregularity = 98%. ¹H NMR and GPC spectra can be found in the Supporting Information.

Device Fabrication: Regioregular P3HT (Rieke Metals, $M_w = 50$ –70 kDa), and IC₆₀BA (Sigma Aldrich, 99% purity) were used as received. ITO-coated aluminosilicate glass slides (Delta Technologies, Ltd.) were cleaned by ultrasonication in acetone and isopropanol for 20 min each, followed by a 10 min UV-ozone plasma treatment. Poly(3,4-ethylenedioxythiophene) poly(styrenesulfonate) (PEDOT:PSS) (H.C. Starck Clevis PH 500) was spin-coated in ambient atmosphere onto the ITO surface at 4000 rpm for 45 s, then annealed for 20 min at 130 °C to produce an approximately 50 nm film. All subsequent fabrication steps were performed in an N₂-filled glovebox. For characterization of the neat polymers, films were spin-cast from chlorobenzene onto the ITO/PEDOT:PSS substrate and annealed for 10 minutes at 150 °C. UV-vis absorption was measured using a PerkinElmer Lambda 750 Spectrophotometer.

Photovoltaic devices were fabricated in the conventional architecture with indium tin oxide (ITO) coated with poly(3,4-ethylenedioxythiophene) poly(styrene-sulfonate) (PEDOT:PSS) as the anode. The active layer consisted of P3HT:ICBA (1:1) as the baseline composition, to which 0 to 20 wt% of P(3HT-*r*-3HOMT) was added, using 1,2-dichlorobenzene (*o*-DCB) as the common solvent for all blend solutions. These films were spin-coated at 800 rpm for 30 s, and then treated with solvent (ca. 30 min) and thermal (150 °C for 10 min) annealing to produce active layer thickness of ca. 180 nm as measured by spectroscopic ellipsometry (M 2000, J.A. Woollam Co.). The cathode consisted of 1 nm LiF and 70 Å Al deposited by vacuum thermal evaporation (Angstrom Engineering); a shadow mask was used to create 1 mm diameter electrodes. Devices were tested in ambient atmosphere under 1 sun illumination (100 mW cm⁻², AM 1.5) using an Oriel solar simulator, and the J–V characteristics were measured using an Agilent 4156C Semiconductor Parameter Analyzer. For photo-CELIV measurements, devices (fabricated in the same manner as described above) were loaded in a cryostat (Janis VPF-100, vacuum pressure 1 mTorr) and exposed to laser pulses (Quantel BrilliantEazy, λ = 532 nm, pulse intensity ca. 20 μJ cm⁻²). A function generator (BK Precision 4075) applied a linearly increasing voltage to extract the photo-generated current transient, which was

passed through a preamplifier (FEMTO DLPCA-200) and recorded by a digital oscilloscope (Tektronix TDS3052C).

Structural Characterization: AFM and KPFM were performed using the Asylum Research MFP-3D. For c-AFM, topography, phase, and dark current were mapped simultaneously in contact mode using a PtIr5-coated probe (NanoWorld) in ambient air, under an applied bias of +3.0 V. KPFM was performed using a platinum silicide-coated probe (Nanosensors) in an argon-filled cell. The probes were calibrated on highly ordered pyrolytic graphite with a work function of 4.6 eV. Surface potentials were measured at a lift height of 10 nm above the sample surface, outside the range of Van der Waals forces.^[56,57] To measure the HOMO energies, samples were prepared on the conventional ITO/PEDOT:PSS substrate (high work function); to measure the LUMO energies, samples were prepared on ITO coated with ~10 nm of ethoxylated polyethyleneimine (PEIE), a low work function substrate.^[58]

EFTEM was performed using a JEOL 2100F TEM, using an accelerating voltage of 200 kV and a slit width of 8 eV. Thinner films (ca. 80 nm) were used for TEM sample preparation to reduce thickness convolution of vertically-overlapping domains/phases. Following the same casting and annealing procedures described previously, the films were sectioned using a razor blade and floated from the substrate by immersion in DI water; the sectioned films were collected onto copper grids with supporting mesh (Ted Pella, Inc.). In performing the EELS measurements, the beam covered a sufficiently large area such that this "overall" EELS represented an averaged spectrum approximating that of a homogeneous mixture. Selected-area local EELS were extracted from spots sampled from multiple different P3HT- and ICBA-rich regions (determined from the EFTEM images) to get a statistically significant values for the plasmon peak energies. These values could be compared to that of the overall EELS to semi-quantitatively compare the relative phase purities of the P3HT- and ICBA-rich domains.

XPS and D-SIMS measurements were performed by Dr. Thomas Mates (Microscopy and Microanalysis Facility at UCSB). XPS was performed with the Kratos Axis Ultra X-ray Photoelectron Spectroscopy System. D-SIMS was performed with the Physical Electronics 6650 Dynamic Secondary Ion Mass Spectrometer using the oxygen ion gun.

Physical data should be quoted with decimal points and negative exponents (e.g., 25.8 JK⁻¹ mol⁻¹), and arranged as follows where possible: mp/bp 20 °C; [α]_D²⁰ = -13.5 (c = 0.2, acetone) (please also give units for [α] and c , usually deg cm³ g⁻¹ dm⁻¹ and g cm⁻³, respectively); ¹H NMR (400 MHz, DMSO-*d*₆, δ): 7.15 (s, 2H, Ar H), 1.3 (q, J = 8 Hz, 2H; CH₂), 0.9 (t, J = 8 Hz, 3H; CH₃); ¹³C NMR (100 MHz, CDCl₃, δ): 175.4 (C = O), 156.5 (C4); IR (KBr): ν = 2972 (w), 2907 (w), ..., 1026 (s; $\nu_{\text{as}}(\text{SiOSi})$), 971 (ν_{s}), ..., 666 (w; $\nu_{\text{s}}(\text{SiOSi})$), ..., 439 (m), 401 cm⁻¹ (m); UV-vis (*n*-hexane): $\lambda_{\text{max}}(\epsilon)$ = 320 (5000), 270 nm (12000); EIMS m/z (%): 108 (20) [M⁺], 107 (60) [M⁺ - H], 91 (100) [C₇H₇⁺]; HRMS (ESI) m/z : [M + H]⁺ calcd for C₂₁H₃₈N₄O₆S, 475.2591; found, 475.2593. Anal. calcd for C₄₅H₂₈N₄O₇: C 62.47, H 3.41, N 6.78; found: C 62.27, H 3.46, N 6.80.

Supporting Information

Supporting Information is available from the Wiley Online Library or from the author.

Acknowledgements

This work was funded as part of the Center for Thermal and Solar Energy Conversion, an Energy Frontiers Research Center supported by the U.S. Department of Energy, Office of Science, Basic Energy Sciences under Award #DE-SC-0000957. We thank Dr. Jonas R. Locke for his contribution to the synthesis of P(3HOMT) and P(3HT-*r*-3HOMT). XPS and SIMS measurements were performed by Dr. Thomas Mates (Microscopy and Microanalysis Facility, UC Santa Barbara). Figure captions were updated on September 17, 2014.

Received: April 2, 2014

Revised: May 8, 2014

Published online: July 14, 2014

- [1] N. D. Treat, M. A. Brady, G. Smith, M. F. Toney, E. J. Kramer, C. J. Hawker, M. L. Chabinyc, *Adv. Energy Mater.* **2011**, *1*, 82.
- [2] N. D. Treat, A. Varotto, C. J. Takacs, N. Batara, M. Al-Hashimi, M. J. Heeney, A. J. Heeger, F. Wudl, C. J. Hawker, M. L. Chabinyc, *J. Am. Chem. Soc.* **2012**, *134*, 15869.
- [3] J. A. Bartelt, Z. M. Beiley, E. T. Hoke, W. R. Mateker, J. D. Douglas, B. A. Collins, J. R. Tumbleston, K. R. Graham, A. Amassian, H. Ade, J. M. J. Fréchet, M. F. Toney, M. D. McGehee, *Adv. Energy Mater.* **2013**, *3*, 364.
- [4] D. Chen, A. Nakahara, D. Wei, D. Nordlund, T. P. Russell, *Nano Lett.* **2011**, *11*, 561.
- [5] W. Ma, J. R. Tumbleston, M. Wang, E. Gann, F. Huang, H. Ade, *Adv. Energy Mater.* **2013**, n/a.
- [6] C. Groves, *Energy Environ. Sci.* **2013**, DOI: 10.1039/C3EE41621F.
- [7] J. Peet, A. J. Heeger, G. C. Bazan, *Acc. Chem. Res.* **2009**, *42*, 1700.
- [8] J. Peet, J. Y. Kim, N. E. Coates, W. L. Ma, D. Moses, A. J. Heeger, G. C. Bazan, *Nat. Mater.* **2007**, *6*, 497.
- [9] J. K. Lee, W. L. Ma, C. J. Brabec, J. Yuen, J. S. Moon, J. Y. Kim, K. Lee, G. C. Bazan, A. J. Heeger, *J. Am. Chem. Soc.* **2008**, *130*, 3619.
- [10] A. Pivrikas, H. Neugebauer, N. S. Sariciftci, *Sol. Energy* **2011**, *85*, 1226.
- [11] G. Li, Y. Yao, H. Yang, V. Shrotriya, G. Yang, Y. Yang, *Adv. Funct. Mater.* **2007**, *17*, 1636.
- [12] L. Chang, H. W. A. Lademann, J.-B. Bonekamp, K. Meerholz, A. J. Moulé, *Adv. Funct. Mater.* **2011**, *21*, 1779.
- [13] J. A. Amonoo, E. Glynos, X. C. Chen, P. F. Green, *J. Phys. Chem. C* **2012**, *116*, 20708.
- [14] A. M. Hiszpanski, L. Loo, *Energy Environ. Sci.* **2013**, DOI: 10.1039/C3EE42615G.
- [15] K. Sivula, Z. T. Ball, N. Watanabe, J. M. J. Fréchet, *Adv. Mater.* **2006**, *18*, 206.
- [16] C. Yang, J. K. Lee, A. J. Heeger, F. Wudl, *J. Mater. Chem.* **2009**, *19*, 5416.
- [17] J. U. Lee, J. W. Jung, T. Emrick, T. P. Russell, W. H. Jo, *Nanotechnology* **2010**, *21*, 105201.
- [18] Z. Sun, K. Xiao, J. K. Keum, X. Yu, K. Hong, J. Browning, I. N. Ivanov, J. Chen, J. Alonzo, D. Li, B. G. Sumpter, E. A. Payzant, C. M. Rouleau, D. B. Geohegan, *Adv. Mater.* **2011**, *23*, 5529.
- [19] C. Renaud, S.-J. Mognier, E. Pavlopoulou, C. Brochon, G. Fleury, D. Deribew, G. Portale, E. Cloutet, S. Chambon, L. Vignau, G. Hadziioannou, *Adv. Mater.* **2012**, *24*, 2196.
- [20] Y. Tao, B. McCulloch, S. Kim, R. A. Segalman, *Soft Matter* **2009**, *5*, 4219.
- [21] R. A. Segalman, B. McCulloch, S. Kirmayer, J. J. Urban, *Macromolecules* **2009**, *42*, 9205.
- [22] N. Sary, F. Richard, C. Brochon, N. Leclerc, P. Lévêque, J.-N. Audinot, S. Berson, T. Heiser, G. Hadziioannou, R. Mezzenga, *Adv. Mater.* **2010**, *22*, 763.
- [23] A. Yassar, L. Miozzo, R. Gironda, G. Horowitz, *Prog. Polym. Sci.* **2013**, *38*, 791.
- [24] E. F. Palermo, H. L. van der Laan, A. J. McNeil, *Polym. Chem.* **2013**, *4*, 4606.
- [25] E. F. Palermo, S. B. Darling, A. J. McNeil, *J. Mater. Chem. C* **2014**, DOI: 10.1039/c3tc32512a.
- [26] L.-M. Chen, Z. Xu, Z. Hong, Y. Yang, *J. Mater. Chem.* **2010**, *20*, 2575.
- [27] Y. S. Eo, H. W. Rhee, B. D. Chin, J.-W. Yu, *Synth. Met.* **2009**, *159*, 1910.
- [28] V. D. Mihaletchi, P. W. M. Blom, J. C. Hummelen, M. T. Rispens, *J. Appl. Phys.* **2003**, *94*, 6849.
- [29] B. Qi, J. Wang, *J. Mater. Chem.* **2012**, *22*, 24315.
- [30] R. Po, C. Carbonera, A. Bernardi, N. Camaioni, *Energy Environ. Sci.* **2011**, *4*, 285.
- [31] G. Heimel, L. Romaner, E. Zojer, J.-L. Brédas, *Nano Lett.* **2007**, *7*, 932.
- [32] C. He, C. Zhong, H. Wu, R. Yang, W. Yang, F. Huang, G. C. Bazan, Y. Cao, *J. Mater. Chem.* **2010**, *20*, 2617.

- [33] H. Wang, E. D. Gomez, Z. Guan, C. Jaye, M. F. Toney, D. A. Fischer, A. Kahn, Y.-L. Loo, *J. Phys. Chem. C* **2013**, DOI: 10.1021/jp406625e.
- [34] Y. He, H.-Y. Chen, J. Hou, Y. Li, *J. Am. Chem. Soc.* **2010**, *132*, 1377.
- [35] G. Zhao, Y. He, Y. Li, *Adv. Mater.* **2010**, *22*, 4355.
- [36] Y.-H. Lin, Y.-T. Tsai, C.-C. Wu, C.-H. Tsai, C.-H. Chiang, H.-F. Hsu, J.-J. Lee, C.-Y. Cheng, *Org. Electron.* **2012**, *13*, 2333.
- [37] S. Ko, E. T. Hoke, L. Pandey, S. Hong, R. Mondal, C. Risko, Y. Yi, R. Noriega, M. D. McGehee, J.-L. Brédas, A. Salleo, Z. Bao, *J. Am. Chem. Soc.* **2012**, *134*, 5222.
- [38] G. H. Fredrickson, J. P. Donley, *J. Chem. Phys.* **1992**, *97*, 8941.
- [39] M. Sikka, N. Singh, A. Karim, F. S. Bates, S. K. Satija, C. F. Majkrzak, *Phys. Rev. Lett.* **1993**, *70*, 307.
- [40] P. Brant, A. Karim, J. F. Douglas, F. S. Bates, *Macromolecules* **1996**, *29*, 5628.
- [41] A. J. Mozer, N. S. Sariciftci, L. Lutsen, D. Vanderzande, R. Österbacka, M. Westerling, G. Juška, *Appl. Phys. Lett.* **2005**, *86*, 112104.
- [42] L. F. Drummy, R. J. Davis, D. L. Moore, M. Durstock, R. A. Vaia, J. W. P. Hsu, *Chem. Mater.* **2011**, *23*, 907.
- [43] D. R. Kozub, K. Vakhshouri, L. M. Orme, C. Wang, A. Hexemer, E. D. Gomez, *Macromolecules* **2011**, *44*, 5722.
- [44] T. P. Russell, *Curr. Opin. Colloid Interface Sci.* **1996**, *1*, 107.
- [45] M. D. Lefebvre, C. M. Dettmer, R. L. McSwain, C. Xu, J. R. Davila, R. J. Composto, S. T. Nguyen, K. R. Shull, *Macromolecules* **2005**, *38*, 10494.
- [46] L. Leibler, *Makromol. Chem. Macromol. Symp.* **1988**, *16*, 1.
- [47] S. H. Anastasiadis, I. Gancarz, J. T. Koberstein, *Macromolecules* **1989**, *22*, 1449.
- [48] D. Kipp, V. Ganesan, *J. Phys. Chem. B* **2014**, *118*, 4425.
- [49] Z. Xu, L.-M. Chen, G. Yang, C.-H. Huang, J. Hou, Y. Wu, G. Li, C.-S. Hsu, Y. Yang, *Adv. Funct. Mater.* **2009**, *19*, 1227.
- [50] A. Maurano, R. Hamilton, C. G. Shuttle, A. M. Ballantyne, J. Nelson, B. O'Regan, W. Zhang, I. McCulloch, H. Azimi, M. Morana, C. J. Brabec, J. R. Durrant, *Adv. Mater.* **2010**, *22*, 4987.
- [51] D. Credgington, J. R. Durrant, *J. Phys. Chem. Lett.* **2012**, *3*, 1465.
- [52] B. P. Lyons, N. Clarke, C. Groves, *Energy Environ. Sci.* **2012**, *5*, 7657.
- [53] D. Ma, M. Lv, M. Lei, J. Zhu, H. Wang, X. Chen, *ACS Nano* **2014**, DOI: 10.1021/nn4059067.
- [54] H. Wang, M. Shah, V. Ganesan, M. L. Chabinyc, Y.-L. Loo, *Adv. Energy Mater.* **2012**, *2*, 1447.
- [55] J. R. Locke, A. J. McNeil, *Macromolecules* **2010**, *43*, 8709.
- [56] H. Hoppe, T. Glatzel, M. Niggemann, A. Hinsch, M. C. Lux-Steiner, N. S. Sariciftci, *Nano Lett.* **2005**, *5*, 269.
- [57] K. Maturová, M. Kemerink, M. M. Wienk, D. S. H. Charrier, R. A. J. Janssen, *Adv. Funct. Mater.* **2009**, *19*, 1379.
- [58] Y. Zhou, C. Fuentes-Hernandez, J. Shim, J. Meyer, A. J. Giordano, H. Li, P. Winget, T. Papadopoulos, H. Cheun, J. Kim, M. Fenoll, A. Dindar, W. Haske, E. Najafabadi, T. M. Khan, H. Sojoudi, S. Barlow, S. Graham, J.-L. Bredas, S. R. Marder, A. Kahn, B. Kippelen, *Science* **2012**, *336*, 327.